Lab on a Chip

PAPER

View Article Online
View Journal | View Issue

Published on 02 April 2015. Downloaded by ECOLE POLYTECHNIC FED DE LAUSANNE on 10/07/2015 12:14:29.

Cite this: *Lab Chip*, 2015, **15**, 2287

Vapor-fed microfluidic hydrogen generator†

M. A. Modestino,* M. Dumortier, S. M. Hosseini Hashemi, S. Haussener, C. Moser and D. Psaltis

Received 5th March 2015,
Accepted 2nd April 2015

DOI: 10.1039/c5lc00259a

www.rsc.org/loc

Water-splitting devices that operate with humid air feeds are an attractive alternative for hydrogen production as the required water input can be obtained directly from ambient air. This article presents a novel proof-of-concept microfluidic platform that makes use of polymeric ion conductor (Nafion®) thin films to absorb water from air and performs the electrochemical water-splitting process. Modelling and experimental tools are used to demonstrate that these microstructured devices can achieve the delicate balance between water, gas, and ionic transport processes required for vapor-fed devices to operate continuously and at steady state, at current densities above 3 mA cm^{-2}. The results presented here show that factors such as the thickness of the Nafion films covering the electrodes, convection of air streams, and water content of the ionomer can significantly affect the device performance. The insights presented in this work provide important guidelines for the material requirements and device designs that can be used to create practical electrochemical hydrogen generators that work directly under ambient air.

Broader context

The large scale deployment of hydrogen production technologies can be triggered by the development of electrolytic devices that function continuously under simple operation schemes. Water-splitting devices that operate under humid air are an attractive alternative to classic alkaline or proton exchange membrane electrolysis systems. In this regard, the implementation of water splitting technologies can be significantly simplified as the water feed could be obtained directly from the environment. Using polymeric ion-conducting materials in a microfluidic platform, this work balances the transport processes that are inherently limiting in devices operated with diluted water feeds, and demonstrates for the first time a vapor-fed microelectrolyzer capable of generating hydrogen at initial current densities above 10 mA cm^{-2}

1. Introduction

A large increase in the share of renewable energy sources for power production is essential to significantly decrease the current levels of CO_2 emissions.[1,2] Large amounts of investment have been allocated to increase the capacities of solar and wind-based power generators. At the same time, power derived from these intermittent sources has brought significant challenges due to their incorporation into our current electricity distribution infrastructure, where electricity generation generally needs to match the demand. Efficient means of power storage and redistribution are needed in order to allow further penetration of renewable energy power production. Electrochemical approaches for power storage by devices such as batteries, flow batteries, electrolyzers and fuel cells exhibit a significant advantage over other means of storage, namely, their efficiency is not limited by the Carnot efficiency of heat engines, as it can reach levels above 70%. Water electrolyzers, in particular, can easily accommodate excess renewable electricity by converting it into hydrogen fuel, which can be stored and subsequently used to regenerate electricity in a fuel cell.[3,4]

Classical electrolysis systems operate under alkaline electrolytes which allow the use of inexpensive and earth-abundant catalysts that operate under basic conditions. These alkaline systems pose significant corrosion challenges for all system components as they require operation under strongly basic electrolytes. More recent approaches to water electrolysis implement membrane electrode assemblies (MEAs) based on proton exchange polymer membranes (PEM) and noble metal catalysts to perform the water splitting process.[5–7] These systems have significant advantages as the ohmic losses through the polymer are minimized by the implementation of thin electrolyte layers, and they are fed with deionized water, alleviating most of the corrosion issues posed by alkaline electrolyzers. One alternative to using deionized water as the feed is to extract water directly from

School of Engineering, École Polytechnique Fédéral de Lausanne (EPFL), Station 17, 1015, Lausanne, Switzerland. E-mail: miguel.modestino@epfl.ch; Tel: +41 21 69 33446

† Electronic supplementary information (ESI) available: Modelling and measurement results of gas crossover, PEIS measurements for devices after steady state operation, device performance measurements under liquid electrolyte, mask design, process flow for device fabrication and AFM characterization of the catalyst surface. See DOI: 10.1039/c5lc00259a

Published on 02 April 2015. Downloaded by ECOLE POLYTECHNIC FED DE LAUSANNE on 10/07/2015 12:14:29.

the vapor phase. Examples of vapor phase water splitting have been demonstrated using MEAs at low temperatures[8] and photoelectrochemical material systems operated directly under air.[9] Performing water electrolysis from the vapor phase exhibits several advantages: lower water splitting potential, lack of bubble evolution at the catalyst surface, and simplified implementation of the electrolyzer by direct humid air-based operation.[9,10] On the downside, water splitting under humid air poses significant transport challenges, as the low concentration of water can limit the water-splitting rates in the device.

The operation of vapor-fed electrolyzers requires all of the ionic current between the reaction sites to be transported by a solid state ion conductor (*i.e.* proton or hydroxide ion conductor). This solid electrolyte needs to satisfy a series of conditions: (i) the electrodes need to be in direct contact with the electrolyte; (ii) the electrolyte needs to have high water solubility as water is consumed in the reaction; (iii) the diffusivity of dissolved H_2 and O_2 gases through the electrolyte needs to be high enough to allow for a product diffusive flux that equates with the production rate at the electrode surface; (iv) the concentration of gases in the electrolyte cannot reach saturation levels in order to avoid bubble nucleation which would cause delamination of the electrolyte; and (v) the water from the environment needs to diffuse with minimum resistance to avoid water depletion at the surface of the electrodes. Nafion thin films are suitable for this task as they provide remarkable ionic conduction, fast water uptake, and good chemical stability.[11–16] Based on Nafion's transport properties, the polymer films covering the electroactive sites must not be thicker than several micrometers to sustain current densities in the electrolyzer in the order of several mA cm^{-2} (1 mA cm^{-2} corresponds to 0.0187 mmol h^{-1} cm^{-2} of H_2 at 100% faradaic efficiency).[17–19,23] Within this thickness range, the in-plane ionic resistance in the polymer can be very significant. One way to mitigate the high resistance is to limit the path length for ion migration between electrodes to short distances, in the order of 10–100 μm. To mitigate these constraints based on Nafion's transport properties, a proof-of-concept microfluidic water-splitting device was fabricated. Microfluidic devices are an attractive platform because their architecture can be easily tuned, their modularity allows for components to be easily exchanged, and the transport characteristics of these devices are well defined. Several studies have focused on the use of microfluidic platforms for fuel cell applications under liquid electrolytes,[20–23] and only recently a microfluidic device was described for water electrolysis in highly acidic (1 M sulphuric acid) electrolytes.[24] To the best of our knowledge, this study presents the first report on microfluidic vapor-fed electrolyzers.

2. Methodology

2.1 Device design

The device presented in this work consists of a set of parallel electrodes covered with a thin layer of Nafion and a set of parallel channels that collect the product gases generated above each of the electrodes. Fig. 1(a) shows a schematic representation of the cross-section of this parallel channel device. In order to maximize the areal coverage of the electrodes in the device, this architecture was arranged in a double spiral geometry (mask designs and process flow are included in the ESI†), allowing maximum coverage of the electrodes in the chip. The double spiral morphology also allowed for independent fluid streams to be collected from the hydrogen and oxygen production channels which prevented the back-diffusion of H_2 into the oxidation side. Fig. 1(b) shows a photograph of the spiral channel structure where water streams with dissolved dyes are flowed through separate streams. It is important to point out that this device architecture is fundamentally different from that of MEAs used in PEM electrolyzers. In MEAs, nanostructured catalyst layers are separated by a parallel ionomer membrane, typically >100 μm thick. In this MEA arrangement, the ionic flux through the membrane is equal to the ionic generation rate in the catalyst layer. In the microfluidic device proposed above, the ionic current is carried through the cross section of an ionomer film of thickness below 1 μm. In this configuration, the ionomer in the inter-electrode region experiences an ionic current density that is more than 125 times higher than that imposed on the catalyst's surface. This results in a

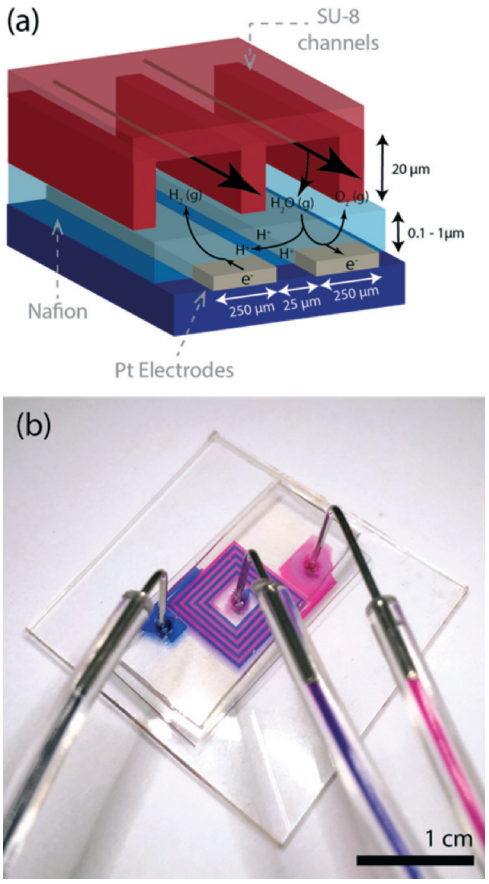

Fig. 1 (a) Diagram of device geometry and (b) fluidic channels showing separate pathways for H_2 (blue) and O_2 (pink) evolution channels.

 This journal is © The Royal Society of Chemistry 2015

Published on 02 April 2015. Downloaded by ECOLE POLYTECHNIC FED DE LAUSANNE on 10/07/2015 12:14:29.

high ionic resistance in the device, and imposes the requirement for short ionic path lengths between the electrodes to minimize the ohmic drop.

2.2 Model development

A steady-state laminar, isothermal 2D model of the microfluidic electrolyzer was developed following modelling methods of proton exchange membrane electrolysis previously established in the literature.[18,25] The model implemented in this study made use of a constant conductivity for the Nafion phase. Variations in the water content throughout the polymer film would lead to a non-uniform conductivity, which is not captured in the current model and can lead to differences between modelling results and experimental measurements.[26] A better understanding of the internal polymer morphology and water uptake throughout the polymer film could lead to more precise models that better describe the experimental systems.[27] The model incorporated the transport phenomena between the two electrodes, the polymeric electrolyte, and the two channels for reactant delivery and product removal, as depicted in Fig. 1(a).[28] The ionomer was considered as an ohmic conductor and as a diffusive medium. The conservation of charge and the species transport in the electrolyte were consequently given by two Laplace equations, assuming spatial constant conductivity and diffusivity of the electrolyte:

$$\Delta V = 0 \tag{1}$$

$$\Delta c_i = 0 \tag{2}$$

The incoming flux of oxygen, water, and hydrogen from the channel to the electrolyte in the direction normal to the catalyst interface is given by,

$$\nabla c_i \cdot \check{\mathbf{n}} = \frac{\mathrm{Sh}\, D_i^{\mathrm{b}}}{e\, D_i^{\mathrm{m}}}\left(c_i - c_i^{\mathrm{b}}\right) \tag{3}$$

where D_i^{b} and D_i^{m} are the diffusion coefficients of species i in the bulk of the air-fed channels and the electrolyte, respectively. $\check{\mathbf{n}}$ is the inward ionomer surface normal, e the height of the channel, and Sh the Sherwood number.

The current densities for the hydrogen evolution and oxygen evolution reactions ($i_{\mathrm{R,OER}}$ and $i_{\mathrm{R,HER}}$) are modeled by using concentration-dependent Tafel approximations,[29]

$$i_{\mathrm{R,OER}} = i_{0,\mathrm{OER}}\left(\frac{c_{\mathrm{H_2O}}}{c_{\mathrm{H_2O}}^{\mathrm{b}}}\right)\exp\left(\frac{\alpha_{\mathrm{a}} F\left(\Phi_{\mathrm{s}} - \Phi_{\mathrm{e}} - E_{\mathrm{O_2/H_2O}}\right)}{RT}\right) \tag{4}$$

$$i_{\mathrm{R,HER}} = -i_{0,\mathrm{HER}}\, a_{\mathrm{H^+}} \exp\left(\frac{\alpha_{\mathrm{c}} F\left(\Phi_{\mathrm{e}} + E_{\mathrm{H^+/H_2}}\right)}{RT}\right) \tag{5}$$

where α_{a} and α_{c} are the charge transfer coefficients at the anode and at the cathode, respectively, and $E_{\mathrm{O_2/H_2O}}$ and $E_{\mathrm{H^+/H_2}}$ are the Nernst potentials of the anodic and cathodic reactions, respectively, with reference concentrations at 20 °C and 1 atm. $i_{0,\mathrm{OER}}$ and $i_{0,\mathrm{HER}}$ are the exchange current densities for the oxygen evolution and hydrogen evolution reactions, F is Faraday's constant and T is the operating temperature. The activity of protons in the electrolyte was fixed by the concentration of sulfonic groups, *i.e.* $a_{\mathrm{H^+}} = 1$. The boundary conditions at the electrode/electrolyte interfaces are given by,

$$\nabla V \cdot \check{\mathbf{n}} = -\frac{i_{\mathrm{R,OER/HER}}}{\sigma} \tag{6}$$

$$\nabla c_{\mathrm{H_2O}} \cdot \check{\mathbf{n}} = \frac{i_{\mathrm{R,OER}}}{2FD_{\mathrm{H_2O}}^{\mathrm{m}}} \tag{7}$$

$$\nabla c_{\mathrm{O_2}} \cdot \check{\mathbf{n}} = -\frac{i_{\mathrm{R,OER}}}{4FD_{\mathrm{O_2}}^{\mathrm{m}}} \tag{8}$$

$$\nabla c_{\mathrm{H_2}} \cdot \check{\mathbf{n}} = \frac{i_{\mathrm{R,HER}}}{2D_{\mathrm{H_2}}^{\mathrm{m}}} \tag{9}$$

The inlet saturation pressure of water vapor was calculated for a relative humidity of one with the correlation from Buck,[30]

$$p_{\mathrm{s}}(T) = 611.21\left(1 + 3.46\times10^{-8} p\right)\exp\left(\frac{17.520T}{240.97 + T}\right) \tag{10}$$

where p is the total pressure. All other external boundaries are considered as walls (no flux conditions). The numerical values of the parameters are given in Table 1. The exchange current densities, anodic charge transfer coefficient and membrane conductivity were calculated to fit the experimental results.

Table 1 Numerical values of the model parameter used in the reference case

Parameter	Value
Diffusion coefficients of water[31–33]	$D_{\mathrm{H_2O}}^{\mathrm{b}} = 0.24\ \mathrm{cm^2\ s^{-1}}$
	$D_{\mathrm{H_2O}}^{\mathrm{m}} = 7.2\times10^{-6}\ \mathrm{cm^2\ s^{-1}}$
Diffusion coefficients of oxygen[26,34,35]	$D_{\mathrm{O_2}}^{\mathrm{b}} = 0.18\ \mathrm{cm^2\ s^{-1}}$
	$D_{\mathrm{O_2}}^{\mathrm{m}} = 5.8\times10^{-7}\ \mathrm{cm^2\ s^{-1}}$
Diffusion coefficients of hydrogen[36,37]	$D_{\mathrm{H_2}}^{\mathrm{b}} = 0.76\ \mathrm{cm^2\ s^{-1}}$
	$D_{\mathrm{H_2}}^{\mathrm{m}} = 1.6\times10^{-6}\ \mathrm{cm^2\ s^{-1}}$
Oxygen concentration in the channels	$c_{\mathrm{O_2}}^{\mathrm{b}} = 0.21\times c^0 = 8.61\ \mathrm{mol^2\ m^{-3}}$
Exchange current densities	$i_{0,\mathrm{HER}} = i_{0,\mathrm{OER}} = 3\times10^{-11}\ \mathrm{A\ cm^{-2}}$
Charge transfer coefficients[38]	$\alpha_{\mathrm{a}} = 0.85$; $\alpha_{\mathrm{c}} = 1$
Membrane conductivity	$\sigma = 4\times10^{-5}\ \mathrm{S\ cm^{-1}}$

Published on 02 April 2015. Downloaded by ECOLE POLYTECHNIC FED DE LAUSANNE on 10/07/2015 12:14:29.

2.3 Device fabrication

The devices were fabricated in the Center of Micronanotechnology at the Swiss Institute of Technology in Lausanne (EPFL). Two separate chip components of the microfluidic devices were fabricated: (1) one chip containing the electrodes and (2) one chip that contained the channel structures. The two chips were subsequently bonded after aligning the channels with the electrodes.

For the electrode fabrication, a lift-off technique was implemented. A 200 nm thermally grown SiO_2 wafer was used to photolithographically pattern the electrode structure in AZ1512 on LOR photoresists (250 μm wide electrodes separated by 25 μm, with a total active length of 10.95 cm). Then, a Leybold Optics LAB 600H e-beam evaporator system was used to deposit 200 nm of platinum (Pt) on top of a 20 nm titanium (Ti) seeding layer, leading to the formation of flat electrode surfaces. To characterize the roughness of the surface, atomic force microscopy measurements were carried using a Bruker Dimension FastScan System (Fig. S7 in the ESI†), which demonstrated a root mean square roughness of 2.2 nm for the metal film. Metal deposition was followed by lift-off in Microposit Remover 1165.

A different process was developed for the fabrication of a set of mixed Pt and iridium oxide (IrO_x) electrodes. First, 200 nm of Pt and 20 nm of Ti were deposited by e-beam evaporation as described above. Then, the cathode structure was photolithographically patterned with AZ1512 photoresists. Ion beam etching (Veeco Nexus IBE350) was used to remove the metal films from areas outside the desired cathode structure, and the remaining photoresist was stripped off using oxygen plasma in a Tepla Gigabatch Plasma Stripper system. A second photolithography step was used to protect the cathode structure with AZ1512 prior to deposition of IrO_x. A 100 nm film of IrO_x was then deposited *via* reactive sputtering, using an Alliance-Concept DP 650 sputtering system, on top of a 150 nm film of chromium (Cr) which acted as a seeding layer to increase the electrical conductivity through the anode. A third lithography step was performed to pattern the anode structure with AZ1512. Lastly, ion beam etching was performed to remove the IrO_x and Cr films from the areas outside the desired anode structure. The remaining photoresist was again stripped off using oxygen plasma.

After removing the excess photoresist with acetone, the chip containing the electrodes was exposed to oxygen plasma for 5 minutes, and Nafion films were spin cast from solutions (15% Nafion solution from ion-power) diluted in isopropanol (Sigma-Aldrich). The film thicknesses were characterized using a Filmetrics F20-UV spectroscopic reflectometer. For the channel fabrication, a 20 μm layer of SU-8 was photolithographically patterned on top of a glass wafer (the channels followed exactly the pattern of the electrodes). After the chip fabrication, both the wafers with electrodes and channels were diced using a Disco DAD321 automatic dicing saw, gas inlet and outlet ports were manually drilled in glass, and the individual chips were aligned under a microscope and bonded at 200 °C (above the glass transition temperatures of Nafion and SU-8). A process flow diagram for all the fabrication steps is included in the ESI.†

2.4 Electrochemical characterization

All the electrochemical measurements were performed using a Biologic VSP-300 potentiostat/galvanostat system. Potentio-electrochemical impedance spectrometry (PEIS) measurements were performed at frequencies between 500 Hz and 3 MHz, and 20 mV amplitude. Impedance results were analysed following electrochemical equivalent circuit models described elsewhere to extract the ohmic resistances of the devices.[14,39] Measurements for equilibrated devices were performed by placing the electrode chips covered with Nafion films in a closed chamber equilibrated with deionized water. The devices were allowed to equilibrate for more than one hour, and measurements were performed when conductivity values reached steady state values. For flow experiments, a New Era syringe pump was used to control the flow rates, and gases were pulled from the outlet while the device inlets were connected to air or nitrogen (N_2) in a container equilibrated with water at ~100% relative humidity (RH).

2.5 Gas composition characterization

Assembled devices were operated by flowing humid air streams saturated with water through the channels at a flow rate of 3 mL h^{-1} using a syringe pump for each of the channels (syringe pumps obtained from New Era). The experiments were run for several hours and gases were collected using gas tight syringes. The sample gases were injected directly into a Bruker 456-GC system with N_2 as the carrier gas to determine the concentration of H_2 in each channel.

3. Results and discussion

Throughout this study, several factors affecting the device performance were assessed, and their effects are presented below. Factors related to transport mechanisms included the effects of ionic, water and gas transport on device behaviour. Additional electrochemical factors such as the reaction kinetic limitations and effects of parasitic oxygen reduction inherent of operation under ambient air were also considered. The findings presented below demonstrate the required balance between the multiple electrochemical and transport processes for optimal air-based operation of water splitting devices.

3.1 Interplay between transport and electrochemical processes

One of the most crucial factors that define the device performance is the ability to provide low transport resistance for both ionic and gas species through the polymer film. In this sense, the thickness of the ionomer films is a crucial parameter and can define the device performance. Thicker films will result in lower ohmic resistances but at the same time will

 This journal is © The Royal Society of Chemistry 2015

Published on 02 April 2015. Downloaded by ECOLE POLYTECHNIC FED DE LAUSANNE on 10/07/2015 12:14:29.

pose larger transport limitations for gas and water diffusion between the electrodes and the flow streams. Modelling results clearly demonstrate that lower ohmic drops are expected as the film thickness increases (Fig. 2(a)). This implies that in devices with thicker Nafion films a larger portion of the applied potential could be used to drive the electrochemical reaction and consequently lead to higher production rates. On the other hand, higher transport resistance for water in thicker films would result in kinetic limitations at the surface of the electrodes as the water concentration decreases. The trade-off between these two effects determines the device current output (Fig. 2(b)).

The balance between the ohmic, mass transport, and reaction kinetics losses also results in inhomogeneities in the current distribution across the electrodes. Reaction kinetic and transport losses drive the system towards a uniform current distribution, while ionic resistances between the electrodes would favour higher current densities at the edges of the electrodes in order to minimize the ionic migration path lengths.[23] As shown in Fig. 3, the current density distribution is uniform at low applied potentials, while anisotropies arise as the potential increases, especially above 2 V. At low applied potentials, the device exhibits low current densities which then lead to a low potential drop of ohmic resistance. As the applied potential increases, the current density in the device reaches levels where the ohmic drop is comparable to the catalyst overpotential. This in turn results in a non-uniform current density distribution, as higher levels of currents are pushed towards electrode areas with the lowest ohmic resistances, *i.e.* the electrode edges. These effects demonstrate the role of multiple transport and chemical processes that are intrinsically present in these complex devices, and the importance of balancing them in order to optimize the performance.

As demonstrated from modelling, proton conduction through the Nafion film is a critical parameter that directly affects the device performance. Potentiostatic electrochemical impedance spectroscopy (PEIS) measurements were performed to characterize the ohmic resistance of devices with Nafion films of various thicknesses (between 300 and 800 nm), and the results are presented in Fig. 4. Within the device architecture used in this study, the derived resistances varied from 140 to 200 ohms, while the contact resistances accounted only for 17 ± 1 ohms for all the devices. The measured resistances in the devices are significant but manageable and demonstrate that devices with thicker electrolyte layers will perform better, as long as water and gas transport through the films

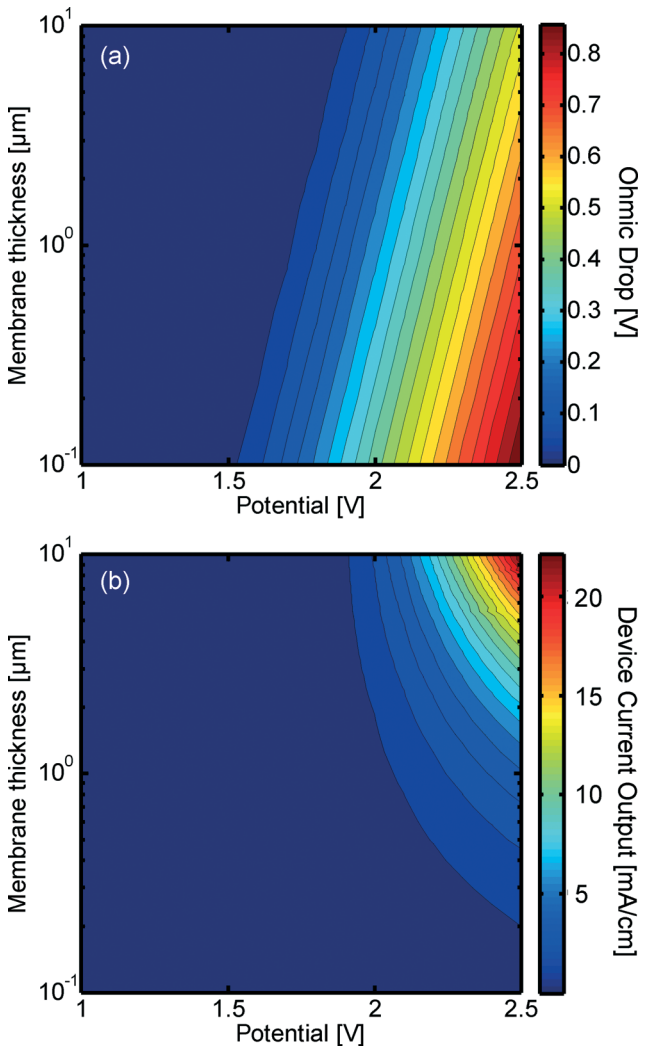

Fig. 2 (a) Ohmic drop in the device as a function of membrane thickness and applied potential. The results show the expected decrease in ohmic losses in the device as the thickness of the ionomer increases. The effect of polymer thickness and applied potential on the device current output is presented in (b). As depicted by the results, the maximum current levels are achieved for a thickness range where the ohmic losses are minimized.

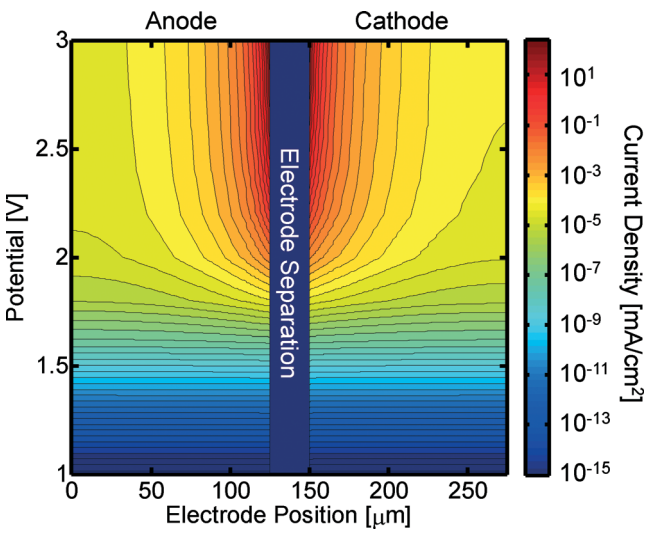

Fig. 3 Current distribution across the electrodes separated by an ionomer layer. The ionomer thickness corresponds to 1 μm, and the anode and cathode center points correspond to electrode positions of 0 and 275 μm, respectively. The non-uniformities observed in the current distribution are caused by the trade-off between the ohmic resistance and reaction kinetic losses.

Published on 02 April 2015. Downloaded by ECOLE POLYTECHNIC FED DE LAUSANNE on 10/07/2015 12:14:29.

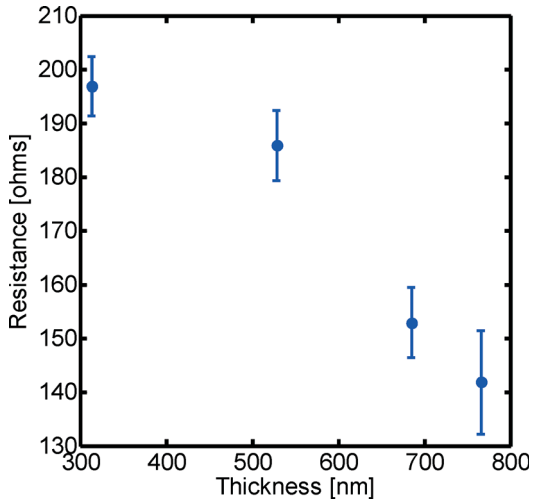

Fig. 4 Device ohmic resistance decreasing as a function of ionomer thickness. The error bars denote standard deviation in the resistance measurements *via* potentiostatic electrochemical impedance.

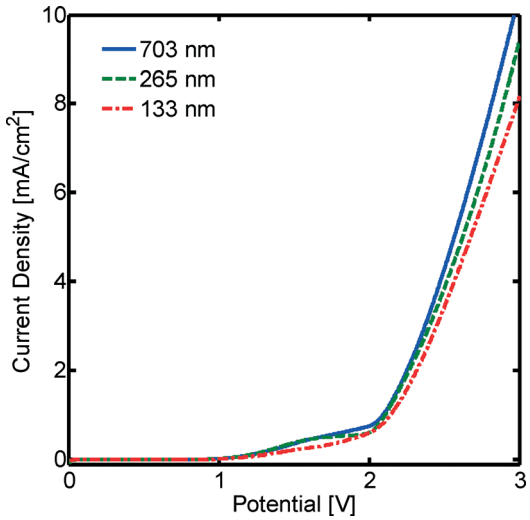

Fig. 5 *I–V* characteristics of devices fabricated with different electrolyte thicknesses, showing performance improvements with thickness as a result of the lower ionic resistance in the device.

does not become limiting. Also, it is important to point out that the measured resistances in these thin films were characterized for electrodes equilibrated in humid air under passive conditions (*i.e.* no flow was applied). These conditions served as a benchmark for comparing devices with different ionomer thicknesses under a controlled set of conditions. Moreover, these devices are expected to show the highest level of performance when the ionomer is fully hydrated after equilibration with humid air. As current is passed through the device, the water concentration in the film over the anode will decrease, and this will lower the conductivity of the material, and increase the ohmic drop in the device.

To better understand the overall performance of the devices, the *I–V* characteristics of the electrodes covered with Nafion were determined after equilibration with 100% RH air (Fig. 5). The traces corresponding to different Nafion thicknesses show a typical behaviour for water electrolysis with Pt electrodes. The region below 2 V where the device exhibits low current levels (below 0.25 mA) is likely to be dominated by kinetic losses in the electrode surface, which arise from catalyst overpotentials. In this region the ohmic drop associated with ionic transport in the electrolyte is expected to be small (<50 mV to 120 mV for films of 703 and 133 nm, respectively), which is why the current levels are not affected significantly by the film thickness. As the applied potential and current increase, the potential requirement for ion transport also increases and starts to become significant. In this regime the film thickness starts to become an important parameter that affects the device performance, and increasing the thickness of the electrolyte allows the device to operate at higher current levels for a given potential.

3.2 Transient device behaviour

The electrochemical characterization presented above provides insights into critical design parameters of the microfluidic electrolyzers. Clearly, the devices presented here benefit from the use of thicker Nafion films which provide lower ionic resistances. Within the range of thicknesses investigated here, significant limitations to the diffusive transport of gases through the electrolyte film are not expected. If devices were to be operated at significantly higher current densities, the concentration of product gases in the electrode/electrolyte interface could reach levels above the gas solubility limit, thus nucleating bubbles and causing the electrolyte film to delaminate.[17,18] Moreover, the characterization described above corresponds to systems that have been equilibrated with humid air and the current levels achieved do not directly correlate with the ones for devices under continuous operation. As current is passed through the electrodes, local concentration gradients of water and gases in the Nafion film will evolve. In the case of the gases generated, the concentration build-up near the electrodes will result in additional overpotentials that need to be overcome. More importantly, the consumption of water inside the ionomer results in two adverse effects for the performance: (i) the decreased water concentration in the Nafion films will lower its conductivity and so increase the device ohmic resistance and (ii) the lower water concentration at the electrode interface will result in lower reaction rates on the catalyst surface. The second effect can be quite severe as the water splitting rate can be limited by the water diffusive flux into the electrodes. Fig. 6 demonstrates the performance drop of devices operated at a constant 3 V applied potential. It can be clearly seen that within the first 5 minutes of operation, the current density in the devices drops sharply and it reaches lower steady state values over time. Moreover, if the flow rates of the feed gas are increased, the steady state current levels also increase. These flow rate effects are consistent with the transport limitations described above, as higher flow rates will increase the convective transport at the polymer/air interface and the water flux into the electrodes will increase. In the same way, the increase in convection will result in a faster flux

 This journal is © The Royal Society of Chemistry 2015

Published on 02 April 2015. Downloaded by ECOLE POLYTECHNIC FED DE LAUSANNE on 10/07/2015 12:14:29.

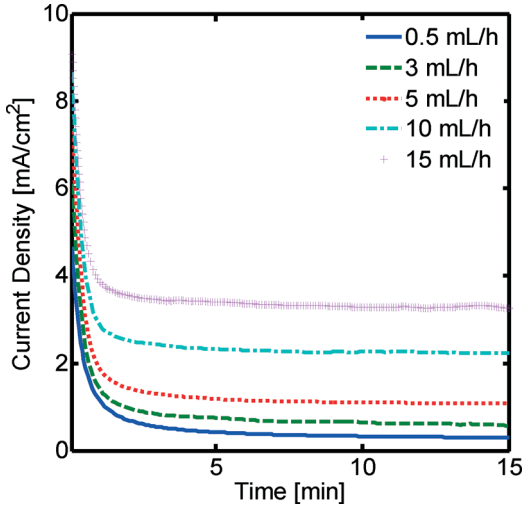

Fig. 6 Current traces for a device with a 700 nm Nafion film operated at 3 V with different feed flow rates. The initial decay in performance suggests that transport limitations arise as the device initially consumes water absorbed in the ionomer, and reaches different current levels at steady state. As the flow rate increases, these transport limitations ease, allowing the device to reach higher current densities.

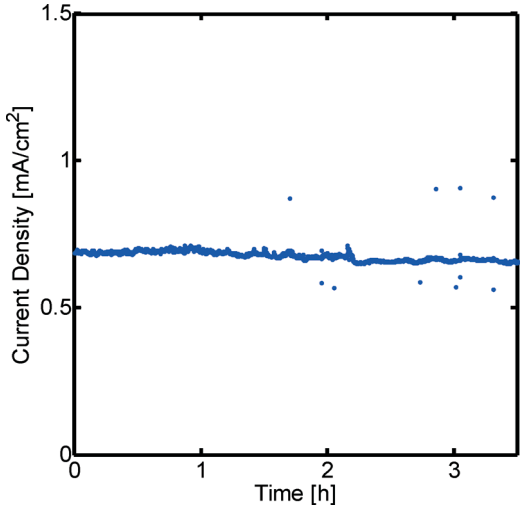

Fig. 7 Long term behaviour of a device with a 700 nm Nafion film operated at steady state with an applied potential of 3 V across electrodes shows stable device operation over the course of several hours.

of gases from the polymer films into the gas streams which in turn will reduce the concentration overpotential at the electrodes. To understand the impact of the decrease in water content in the Nafion film, PEIS measurements were performed after the device had achieved steady state (Fig. S3 in the ESI†) operation and the resistances in the devices were found to increase from ~200 ohms to at least 800 ohms in the case of a flow rate of 15 mL h^{-1} and above 6000 ohms for the lowest flow rate of 0.5 mL h^{-1}. These resistance levels will result in large ohmic drops in the device, >800 mV for devices operated at 1 mA with a feed flow rate of 15 mL h^{-1}.

Although the initial performance of the devices decreases with time due to the transient effects described above, their performance at steady state is stable over several hours. Fig. 7 demonstrates the stable steady state behaviour of a device operated at 3 V with a total air flow rate of 3 mL h^{-1} per channel. Moreover, the device used to perform the measurements presented below has been used for over a month under varying operating conditions and does not show signs of performance degradation. Both the electrode materials (Pt) and the ionomer (Nafion) show remarkable electrochemical stability, as is the case for these materials in MEAs used in fuel cells and electrolyzers. This suggests that the devices described herein can be potentially operated over long periods of time.

3.3 Gas transport across channels

Electrolytic devices need to limit the hydrogen crossover from the reduction to the oxidation channels in order to avoid product losses, especially by product recombination at the surface of the anode. It must be noted that downstream separation of the hydrogen gas is still required as its concentration in the product stream is expected to be low if the device is operated directly under humid air. Coupled mass transport and electrochemical models were developed to assess the degree of gas crossover through the Nafion film. Additionally, gas chromatography measurements were used to determine the extent of hydrogen back diffusion. In the devices described above, diffusion of H_2 across the channels can happen through the Nafion thin film that ionically connects the two electrodes. As the thickness of the films used lies below 1 μm, the H_2 crossover through the Nafion films is expected to be low. Modelling results demonstrate that the concentration of H_2 reaching the oxidation side corresponded to less than 1% of that produced in devices with Nafion thicknesses below 1 μm (Fig. S1 in the ESI†). These results suggest that the thickness of the film can be optimized without affecting the gas crossover in the device. Experimental results of the device modelled here demonstrated low levels of crossover, as 97% of the H_2 in the system was collected in the reduction side, and 3% of it was collected in the oxygen side (GC results are presented in the ESI†). Cross-contamination at the inlets and outlets of the demonstration device, imperfections in the bonding between Nafion and the channel walls, as well as non-zero diffusion of H_2 through the SU-8 walls could result in the higher measured H_2 crossover when compared to the model estimations. It is important to point out that crossover of oxygen from the oxidation to the reduction channels can have similar detrimental effects due to recombination losses in the cathode. In the case of the devices presented in this study, the crossover of oxygen is expected to be lower than that measured for H_2, as its permeability in Nafion is lower.[40,41]

3.4 Parasitic reduction of atmospheric oxygen

It is important to point out that this study focused on the operation of devices under humid air, and the presence of O_2

Published on 02 April 2015. Downloaded by ECOLE POLYTECHNIC FED DE LAUSANNE on 10/07/2015 12:14:29.

in the feed can have several drawbacks in the performance of the devices. When electrolytic devices are operated in the presence of air, the oxygen reduction reaction can compete with the hydrogen evolution reaction in the cathode, and the measured current output arises from both reactions. To assess the extent of this effect, current–voltage characteristics were measured for devices operated under humid air and humid N_2 (100% RH) as depicted in Fig. 8. It can be noted that higher current densities are obtained when air (up to 19% higher at 3 V) is present in the feed stream. Similar effects have been reported elsewhere for the case of air-operated MEAs.[8] Furthermore, the presence of oxygen in the H_2 stream can result in recombination losses, and a more complex downstream separation of the gases will be required to obtain pure H_2 fuel. The electrochemical model presented earlier follows the behaviour of the nitrogen-fed device, further confirming the presence of additional parasitic reactions occurring in the electrodes when oxygen is present. Under humid N_2, these parasitic electrode reactions are not present and the faradaic efficiency of the devices is expected to approach 100%. Given these conditions, the energy conversion efficiency at different current density levels can be estimated. Fig. S8 in the ESI† presents a trace of the current density in the device as a function of efficiency, demonstrating that the device can operate at current densities above 2.5 mA cm^{-2} with efficiencies higher than 50%.

3.5 Improving the reaction kinetics at the electrodes

The previous subsections discussed the interplay of multiple transport processes that play important roles in the performance of vapor operated electrolyzers, and highlighted directions for improvements in the device current outputs. While

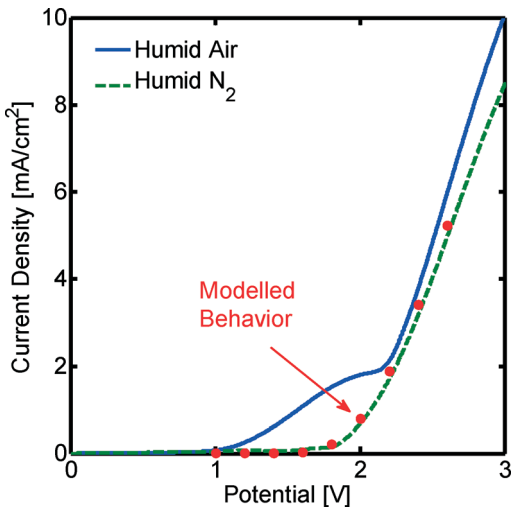

Fig. 8 Electrochemical behaviour of a device operated with a feed flow rate of 15 mL h^{-1} of humid air (solid line) or nitrogen (dashed line). The results demonstrate higher current densities in the presence of oxygen due to parasitic recombination reactions in the cathode. The current density values for the nitrogen-fed system compare well with modelling results, presented as red dots in the graph.

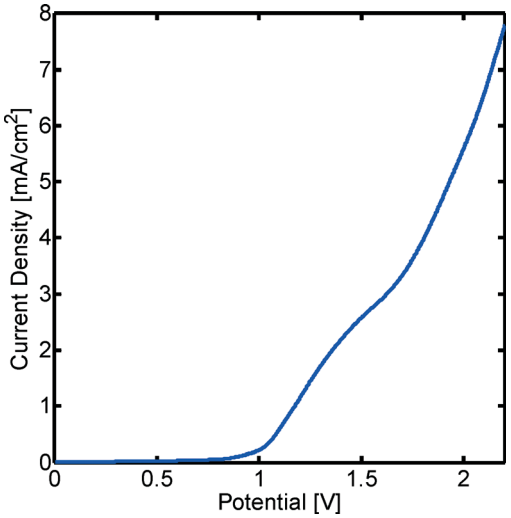

Fig. 9 *I–V* characteristics of a set of Pt and IrO_x electrodes covered with a 700 nm film of Nafion. The use of IrO_x in the anodic reaction leads to a decrease in overpotential in the device.

the devices described above used Pt as an electrocatalyst for both the oxygen and hydrogen evolution reactions, further gains can be attained by implementing catalysts with lower overpotentials. To demonstrate the performance improvements from the incorporation of catalysts with higher activity, a set of electrodes were fabricated with IrO_x as the water oxidation catalyst and Pt for the proton reduction reaction. This catalyst combination is widely used in PEM electrolyzers as it allows MEAs to operate at lower potentials and with improved stability.[6] As demonstrated in Fig. 9, significantly lower overpotentials can be achieved when IrO_x is used in the anodic reaction. Average current densities above 5 mA cm^{-2} are observed at 2 V of applied potentials, compared to less than 2 mA cm^{-2} in systems that used Pt for the oxygen evolution reaction. The recorded improvement is significant, and demonstrates that the incorporation of better catalysts leads to more efficient device operation.

4. Conclusions

The platform developed in this study demonstrates for the first time a room-temperature water-vapor microfluidic electrolyzer. This system allowed for thorough electrochemical characterization of device architectures to gain insights into the effects of various design parameters on the performance of water-vapor electrolyzers. The findings of our study demonstrate the interplay of the multiple transport processes required for optimal device behaviour. In particular, ion-transport resistance in these devices can dominate their electrochemical behaviour; the measured resistance levels (>200 ohms) can account for a large portion of the overpotential required for the water splitting reaction (>200 mV at 1 mA current outputs). Moreover, under steady state operating conditions, the ionic resistance in the device can increase significantly (by more than 400%) due to water consumption at the anode

 This journal is © The Royal Society of Chemistry 2015

Published on 02 April 2015. Downloaded by ECOLE POLYTECHNIC FED DE LAUSANNE on 10/07/2015 12:14:29.

and concentration overpotentials may arise from the evolution of product gases near the electrodes. These effects can be partially mitigated by increasing the convection at the gas/electrolyte interface and in this way increase the convective mass transfer, improving the efficiency of the device. It must be noted that although Nafion films have desirable properties such as high proton conduction and electrochemical stability, its gas permeability is fairly low. This property is desirable for membranes in classic fuel cell and electrolyzer designs where gas crossover can affect the performance of devices, but for the vapor-fed water splitting devices described here, higher gas permeability and water uptake could ease the transport limitations. Also, contrary to catalyst layers in MEAs, this study implemented planar electrodes with active catalyst areas limited to the projected areas of the electrodes. Further studies should focus on nanostructuring the surface of electrocatalysts in order to significantly increase the device current output. The insights and design rules presented in this study can pave the way for the development of high current density electrolysis or solar-hydrogen reactors[9,17,18,42] that operate directly under ambient air.

Acknowledgements

This material is based on work performed with financial support from the Nano-Tera.ch initiative, as part of the Solar Hydrogen Integrated Nano Electrolysis project (contract # 530 101). The authors would also like to thank Yannick Gaudy, Dr. Jay-Woo Choi and Dr. Donald Conkey for helpful discussions, as well as Laszlo Petho for assistance with the microfabrication process.

Notes and references

1 S. Chu and A. Majumdar, *Nature*, 2012, **488**, 294–303.
2 N. S. Lewis and D. G. Nocera, *Proc. Natl. Acad. Sci. U. S. A.*, 2006, **103**, 15729–15735.
3 C. A. Rodriguez, M. A. Modestino, D. Psaltis and C. Moser, *Energy Environ. Sci.*, 2014, **7**, 3828–3835.
4 B. A. Pinaud, J. D. Benck, L. C. Seitz, A. J. Forman, Z. Chen, T. G. Deutsch, B. D. James, K. N. Baum, G. N. Baum, S. Ardo, H. Wang, E. Miller and T. F. Jaramillo, *Energy Environ. Sci.*, 2013, **6**, 1983–2002.
5 K. E. Ayers, E. B. Anderson, C. Capuano, B. Carter, L. Dalton, G. Hanlon, J. Manco and M. Niedzwiecki, *ECS Trans.*, 2010, **33**, 3–15.
6 M. Carmo, D. L. Fritz, J. Mergel and D. Stolten, *Int. J. Hydrogen Energy*, 2013, **38**, 4901–4934.
7 M. K. Debe, *ECS Trans.*, 2012, **45**, 47–68.
8 J. M. Spurgeon and N. S. Lewis, *Energy Environ. Sci.*, 2011, **4**, 2993–2998.
9 J. Ronge, S. Deng, S. Pulinthanathu Sree, T. Bosserez, S. W. Verbruggen, N. Kumar Singh, J. Dendooven, M. B. J. Roeffaers, F. Taulelle, M. De Volder, C. Detavernier and J. A. Martens, *RSC Adv.*, 2014, **4**, 29286–29290.
10 M. A. Modestino and S. Haussener, *Annu. Rev. Chem. Biomol. Eng.*, 2015, 6, DOI: 10.1146/annurev-chembioeng-061114-123357, In Press.
11 K. A. Mauritz and R. B. Moore, *Chem. Rev.*, 2004, **104**, 4535–4585.
12 A. Kusoglu, M. A. Modestino, A. Hexemer, R. A. Segalman and A. Z. Weber, *ACS Macro Lett.*, 2011, **1**, 33–36.
13 M. A. Modestino, A. Kusoglu, A. Hexemer, A. Z. Weber and R. A. Segalman, *Macromolecules*, 2012, **45**, 4681–4688.
14 M. A. Modestino, D. K. Paul, S. Dishari, S. A. Petrina, F. I. Allen, M. A. Hickner, K. Karan, R. A. Segalman and A. Z. Weber, *Macromolecules*, 2013, **46**, 867–873.
15 D. K. Paul, A. Fraser, J. Pearce and K. Karan, *ECS Trans.*, 2011, **41**, 1393–1406.
16 S. A. Eastman, S. Kim, K. A. Page, B. W. Rowe, S. Kang, C. L. Soles and K. G. Yager, *Macromolecules*, 2012, **45**, 7920–7930.
17 M. R. Singh, J. C. Stevens and A. Z. Weber, *J. Electrochem. Soc.*, 2014, **161**, E3283–E3296.
18 C. Xiang, Y. Chen and N. S. Lewis, *Energy Environ. Sci.*, 2013, **6**, 3713–3721.
19 A. Berger, R. A. Segalman and J. Newman, *Energy Environ. Sci.*, 2014, **7**, 1468–1476.
20 E. Kjeang, N. Djilali and D. Sinton, *J. Power Sources*, 2009, **186**, 353–369.
21 E. R. Choban, L. J. Markoski, A. Wieckowski and P. J. A. Kenis, *J. Power Sources*, 2004, **128**, 54–60.
22 S. M. Mitrovski, L. C. C. Elliott and R. G. Nuzzo, *Langmuir*, 2004, **20**, 6974–6976.
23 S. Haussener, S. Hu, X. Chengxiang, A. Z. Weber and N. Lewis, *Energy Environ. Sci.*, 2013, **6**, 3605–3618.
24 M. A. Modestino, C. A. Diaz-Botia, S. Haussener, R. Gomez-Sjoberg, J. W. Ager and R. A. Segalman, *Phys. Chem. Chem. Phys.*, 2013, **15**, 7050–7054.
25 P. K. Das, X. Li and Z.-S. Liu, *J. Electroanal. Chem.*, 2007, **604**, 72–90.
26 H. Ito, T. Maeda, A. Nakano and H. Takenaka, *Int. J. Hydrogen Energy*, 2011, **36**, 10527–10540.
27 M. Schalenbach, M. Carmo, D. L. Fritz, J. Mergel and D. Stolten, *Int. J. Hydrogen Energy*, 2013, **38**, 14921–14933.
28 J. Newman and K. Thomas-Alyea, *Electrochemical Systems*, Wiley & Sons, 2004.
29 A. J. Bard and L. R. Faulkner, *Electrochemical Methods, Fundamentals and Applications*, Wiley & Sons, 2000.
30 A. L. Buck, *J. Appl. Meteorol.*, 1981, **20**, 1527–1532.
31 Q. Zhao, P. Majsztrik and J. Benziger, *J. Phys. Chem. B*, 2011, **115**, 2717–2727.
32 T. R. Marrero and E. A. Mason, *J. Phys. Chem. Ref. Data*, 1972, **1**, 3–118.
33 J. Kestin, K. Knierim, E. A. Mason, B. Najafi, S. T. Ro and M. Waldman, *J. Phys. Chem. Ref. Data*, 1984, **13**, 229–303.
34 A. T. Haug and R. E. White, *J. Electrochem. Soc.*, 2000, **147**, 980–983.
35 V. A. Sethuraman, S. Khan, J. S. Jur, A. T. Haug and J. W. Weidner, *Electrochim. Acta*, 2009, **54**, 6850–6860.
36 T. Sakai, H. Takenaka and E. Torikai, *J. Electrochem. Soc.*, 1986, **133**, 1–5.

Published on 02 April 2015. Downloaded by ECOLE POLYTECHNIC FED DE LAUSANNE on 10/07/2015 12:14:29.

37 R. Nagahisa, D. Kuriya, K. Ogawa, Y. Takata and K. Ito, *ECS Trans.*, 2011, **41**, 1423–1430.
38 J. O. M. Bockris, A. Ammar and S. Huq, *J. Phys. Chem.*, 1957, **61**, 879–886.
39 D. K. Paul, A. Fraser and K. Karan, *Electrochem. Commun.*, 2011, **13**, 774–777.
40 J. S. Chiou and D. R. Paul, *Ind. Eng. Chem. Res.*, 1988, **27**, 2161–2164.
41 A. Z. Weber and J. Newman, *J. Electrochem. Soc.*, 2004, **151**, 311–325.
42 S. Y. Reece, J. A. Hamel, K. Sung, T. D. Jarvi, A. J. Esswein, J. J. H. Pijpers and D. G. Nocera, *Science*, 2011, **334**, 645–648.

 This journal is © The Royal Society of Chemistry 2015